Towards Direction-Equilibrated Segmentation in 3D Medical Images

Zhiqin Zhu[1], Keyu Pu[1], Yu Liu[2(✉)], Guanqiu Qi[3], Yan Ding[1], and Baisen Cong[4]

[1] College of Automation, Chongqing University of Posts and Telecommunications, Chongqing, China
[2] Department of Biomedical Engineering and Anhui Province Key Laboratory of Measuring Theory and Precision Instrument, Hefei University of Technology, Hefei, China
[3] Computer Information Systems, State University of New York College at Buffalo, Buffalo, NY, USA
[4] Department of Clinical Oncology, Queen Elizabeth Hospital, Hong Kong, China
yuliu@hfut.edu.cn

Abstract. Due to structural anisotropy and complex anatomical boundaries, 3D medical image segmentation remains a challenging task. To address these issues, this paper proposes the Direction-Sensitive Equilibrium Mamba Network (DEM-Mamba). Through directional decoupling, balanced enhancement, and adaptive fusion, this network systematically enhances structure perception and boundary preservation capabilities in 3D space. Specifically, DEM-Mamba integrates three core designs: First, it employs an Orientation-Aware Module (OAM) based on learnable Riesz wavelets to decouple high-frequency directional features and mitigate information imbalance caused by anisotropic resolution. Second, it designs a Bidirectional Balanced Mamba (BBM), which effectively captures long-range anisotropic dependencies and maintains boundary clarity through complementary bidirectional scanning combined with adaptive normalization. Finally, it introduces an Orientation-Conflict Fusion (OCF) mechanism that dynamically aggregates multi-directional information based on correlation weights, enhancing the model's adaptability to complex boundaries. Experiments across multiple 3D medical image datasets demonstrate that this method outperforms existing state-of-the-art approaches in both segmentation accuracy and boundary integrity, providing an effective new framework for 3D medical image segmentation. Code is available at https://github.com/pky888/DEM-Mamba

Keywords: 3D medical image segmentation · Mamba · Wavelet.

1 Introduction

3D medical image segmentation is essential for precise clinical diagnosis and treatment planning[1, 2]. However, such images exhibit significant structural anisotropy, with anatomical features unevenly distributed across directions. Particularly along the low-resolution acquisition axis, gradual gray-level transitions

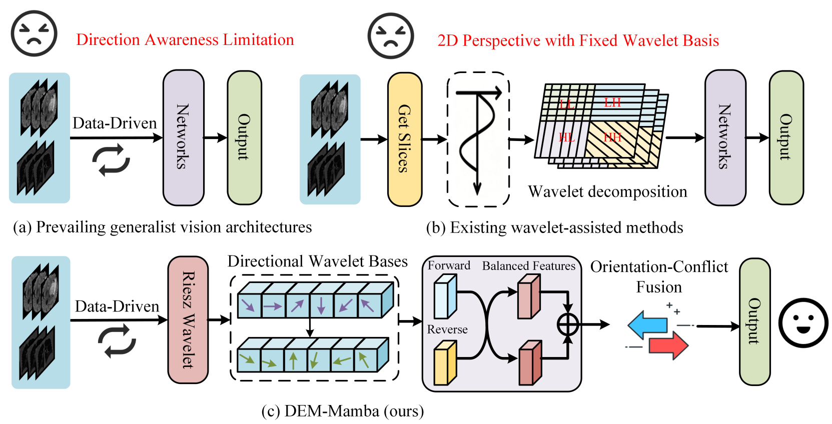

Fig. 1: Conceptual comparison: limitations of generalist vision architectures (a) and 2D fixed-wavelet methods (b) versus the proposed DEM-Mamba framework with learnable directional decoupling, global equilibrium enhancement, and adaptive multi-feature aggregation (c).

and blurred edges severely hinder accurate boundary delineation. Current methods fall short in addressing these anisotropic challenges: CNNs are limited by local receptive fields, Transformers incur high computational costs without explicit anisotropy modeling[3], and Mamba's fixed 1D scanning disrupts spatial continuity, leading to inadequate fuzzy boundary capture. Collectively, existing approaches lack systematic directional perception and modeling of anisotropic structures, constituting a major bottleneck for accurate 3D segmentation[4, 5].

Although the wavelet transform offers a powerful multiscale and multidirectional framework to address limitations in directional perception, existing approaches suffer from two major shortcomings: most are limited to 2D slice-wise processing, failing to ensure directional consistency across 3D volumes, and they rely on fixed basis functions (e.g., Haar wavelets) without learnable parameterization, reducing adaptability to diverse anatomical patterns. These flaws hinder deep integration with modern deep learning frameworks and limit breakthrough performance in complex 3D segmentation tasks[6, 7].

To address boundary degradation from anisotropic structures in 3D medical images, this paper proposes the Direction-Sensitive Equilibrium Mamba Network (DEM-Mamba). As shown in Fig.1, DEM-Mamba follows a "direction decoupling–equilibrium modeling–adaptive aggregation" pipeline with three core modules: Orientation-Aware Module (OAM) extracts and enhances multi-directional boundary features via learnable 3D Riesz wavelet transform; Bidirectional Balanced Mamba (BBM) establishes complementary bidirectional state flows for mutually enriching multi-directional fusion and linear-complexity long-range context modeling; Orientation-Conflict Fusion (OCF) dynamically adjusts aggregation weights based on feature correlation to maintain boundary integrity.

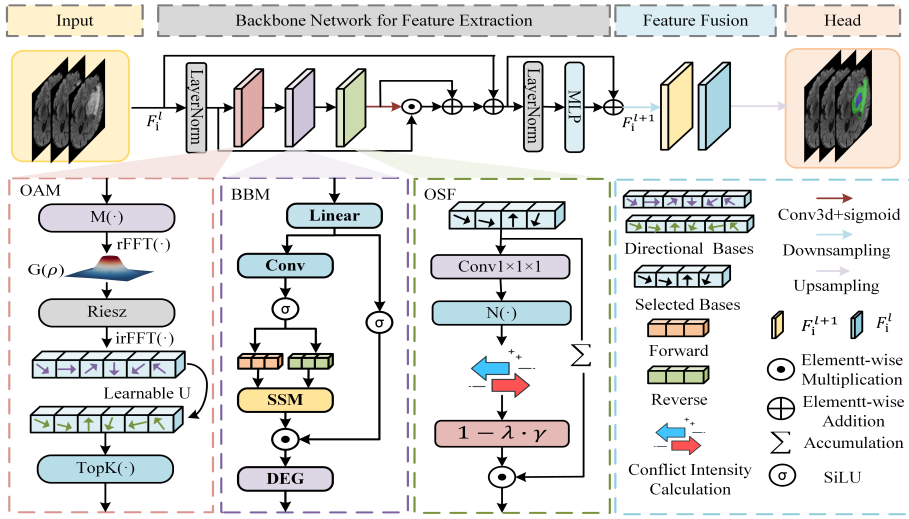

Fig. 2: DEM-Mamba Overall Framework Diagram, where F_i^l denotes the input features of layer l, with $l \in \{1, 2, 3, 4\}$.

The key innovations are: (1) the unified DEM-Mamba framework that deeply integrates direction-adaptive perception with state space modeling, introducing a novel paradigm for anisotropic boundary modeling; (2) the OAM, BBM, and OCF modules that systematically enable direction-sensitive decoupling, long-range complementary balanced fusion, and adaptive conflict suppression; and (3) superior performance over state-of-the-art methods on four 3D medical datasets.

2 Methods

2.1 Overview

As illustrated in Fig. 2, the proposed DEM-Mamba framework progressively extracts and refines semantic features via three cascaded modules. The OAM uses learnable Riesz wavelets for multi-directional decomposition to capture direction-sensitive boundary primitives. The BBM applies complementary forward-backward scanning on directional components to model long-range dependencies and ensure boundary consistency. The OCF dynamically fuses multi-directional features with adaptive weighting to suppress conflicts while preserving structural integrity. Final multi-layer fusion via transposed convolutions and skip connections yields the segmentation output.

2.2 Orientation-Aware Module

To overcome the limited anisotropic perception in existing 3D medical imaging models, we propose the OAM. Inspired by frequency-domain directional separation using Riesz transform filter banks [8], OAM employs a learnable steering mechanism based on higher-order Riesz transforms to construct a continuously steerable directional representation. For input features, it computes direction-sensitive boundary primitives as follows:

$$F_{dir} = irFFT(rFFT(M(F_{in})) \odot G(\rho) \odot \hat{R}^n(\omega)), \tag{1}$$

where $M(\cdot)$ extracts multi-scale features via dilated separable convolutions with rates, equipped with a global channel-weighting branch. $rFFT(\cdot)$ and $irFFT(\cdot)$ denote the real-valued FFT and its inverse. $\odot$ is element-wise multiplication. $G(\rho)$ is a radial log-Gabor filter for high-frequency extraction. The high-order Riesz transform $\hat{R}^n(\omega) = (-j)^N \sqrt{\frac{N!}{n!}} \frac{\omega^n}{|\omega|^N}$ provides directional basis, with the multi-index $n = (n_W, n_H, n_D)$ satisfies $|n|_1 = N$ and yields M directional basis. A learnable transformation matrix $U \in \mathbb{R}^{M \times M}$ is further adopted to adaptively reorganize directional features for better matching anatomical structures:

$$F_{dir}^{'} = U \cdot F_{dir}, \tag{2}$$

where F_{dir} and F'_{dir} represent the original and reconstructed directional component stacks, respectively. Given the unequal local contributions of directional components, we introduce an energy-based Top-K routing mechanism. It adaptively isolates the K highest-energy directions, enhancing dominant structural information while efficiently preserving critical anisotropic details:

$$F''_{dir} = TopK(\|F'_{dir,C,D,H,W}\|^2)_K, \tag{3}$$

where the energy calculation is based on the squared norm of the channel (C), depth (D), height (H), and width (W) dimensions. The Top-K components are selected to form the final output F''_{dir}.

2.3 Bidirectional Balanced Mamba

To enhance long-range modeling of heterogeneous structures, we propose the BBM model. It utilizes complementary bidirectional scanning and adaptive normalization, along with a novel Dual-Equal Gate (DEG) module, to accurately preserve high-frequency boundary details while ensuring global semantic coherence.

(a)Bidirectional Mamba. Avoiding exhaustive 3D sweeps, BBM exclusively scans Top-K dominant components for efficiency. This bidirectional choice is pragmatic, not a theoretical rejection of multi-path designs. The state-space equation is:

$$\begin{cases} h_t^f = Ah_{t-1}^f + Bx_t, \\ h_t^r = Ah_{t+1}^r + Bx_t, \\ y_t^{f,r} = Ch_t^{f,r} + Dx_t, \end{cases} \tag{4}$$

where A, B, C, and D are learnable parameter matrices. During the forward pass, the hidden state h_t^f is recursively computed from the state at the previous time step t-1. In the reverse pass, the hidden state h_t^r is recursively derived from the state at the subsequent time step t+1. x_t and $y_t^{f,r}$ represent the input state and output state, respectively.

(b)Dual-Equal Gate. We propose DEG to suppress out-of-phase destructive interference and enhance in-phase constructive superposition after bidirectional Mamba scanning. For the bidirectional Mamba learning results $X_{f,r}$:

$$u_{f,r} = \phi(X_{f,r}), \tag{5}$$

where $\phi(\cdot)$ denotes a 3×3×3 depthwise separable convolution, GELU activation, pointwise convolution, and a fast 3D channel attention module[9]. Soft selection weights are given by:

$$\alpha, \beta = Softmax(Conv_{c\to 2}(u_f + u_r), dim = 1), \tag{6}$$

where $\alpha+\beta = 1$. $Conv_{c\to 2}(\cdot)$ performs channel compression to 2, and $Softmax(\cdot)$ denotes the softmax operation. The final output Y is:

$$Y = [\alpha \odot u_f \odot \sigma(\beta \odot u_r)] + [\beta \odot u_r \odot \sigma(\alpha \odot u_f)], \tag{7}$$

where σ is sigmoid.The design suppresses phase cancellation, enhances feature consistency, speeds up inference, and stabilizes training.

2.4 Orientation-Conflict Fusion

Due to destructive interference (phase conflicts) during superposition, multi-directional high-frequency components often experience energy cancellation, which degrades the fusion quality. Inspired by the inclusion-exclusion principle[10], we propose the OCF mechanism to perform conflict-aware fusion on BBM-enhanced Top-K components $\{h_i\}_{i=1}^K$.

Each directional feature h_i is projected via 1×1×1 convolution and InstanceNorm3d (N($\cdot$), with learnable affine parameters) to get p_i. The channel-wise global mean vector u_i is computed over $[D, H, W]$:

$$p_i = N(\mathrm{Conv}_{1\times1\times1}(h_i)), \quad u_i = \mathrm{mean}_{[D,H,W]}(p_i), \tag{8}$$

The global conflict intensity $\gamma \in [0, 1]$ across all components is quantified as:

$$\gamma = \frac{2}{K(K-1)} \sum_{i<j} max(0, tanh(\frac{< p_i - u_i, p_j - u_j >}{\|p_i - u_i\| \, \|p_j - u_j\| \cdot \tau})), \tag{9}$$

where the learnable temperature τ adaptively controls conflict detection sensitivity. Low values of γ reflect directional phase coherence, whereas high values indicate pronounced destructive interference.

The final fused representation is obtained through conflict-modulated summation:

$$OSF(\{h_i\}_{i=1}^K) = (\sum_{i=1}^{K} h_i) \odot (1 - \lambda \cdot \gamma), \tag{10}$$

Table 1: Comparison of Different Methods on BraTS2023 and AIIB2023 Datasets

Methods	BraTS2023						AIIB2023		
	Dice(%) ↑			HD95(mm) ↓			Airway-Tree		
	ET	TC	WT	ET	TC	WT	IoU ↑	DLR ↑	DBR ↑
nnU-Net[11]	83.52	89.52	92.69	4.61	5.02	5.31	87.02	61.28	50.31
TransUNet[12]	83.95	88.52	92.15	4.50	4.36	6.23	86.57	62.35	48.62
UNETR[13]	84.47	86.37	92.17	5.01	5.29	6.15	83.20	48.01	38.71
Swin UNETR[14]	84.19	87.77	92.69	4.46	4.41	5.21	87.15	63.33	52.17
MedNeXt[15]	83.92	87.72	92.38	4.49	4.66	4.96	85.82	57.46	47.36
SwinUNETR-V2[16]	85.16	89.64	93.33	5.02	4.42	4.42	87.52	46.02	53.21
UltraLight VM-UNet[17]	79.30	86.23	91.38	5.27	6.15	5.63	82.51	46.02	37.03
VSMU-Net[18]	87.72	92.66	93.63	**2.86**	3.27	3.38	88.58	70.22	61.28
Proposed	**87.74**	**92.76**	**93.78**	3.30	**3.15**	**3.24**	**88.71**	**71.03**	**61.60**

Table 2: Comparison of Different Methods on BraTS2024 Datasets.

Method	WT		TC		ET		RC	
	Dice	HD95	Dice	HD95	Dice	HD95	Dice	HD95
nnU-Net[11]	88.20	4.58	75.71	5.18	71.81	4.14	62.12	6.15
TransUNet[12]	87.32	5.19	76.60	8.06	71.33	3.07	63.11	8.86
UNETR[13]	85.34	12.79	67.92	14.79	61.33	7.93	51.07	15.72
Swin Transformer[19]	82.31	10.60	66.13	12.29	57.42	6.44	49.51	10.92
TransBTS[20]	82.41	10.90	61.33	9.29	55.12	8.64	45.42	9.56
NestedFormer[21]	88.12	4.13	76.62	**4.04**	66.51	4.52	61.82	4.64
nnFormer[22]	85.21	4.64	70.42	6.06	76.62	3.17	53.52	6.47
AAHN[23]	89.72	3.56	**78.52**	4.24	73.01	**2.77**	65.52	5.02
Proposed	**89.86**	**3.42**	70.56	5.57	**79.23**	3.16	**77.34**	**3.95**

where the suppression strength is governed by scalar λ. When directional conflict is severe ($\gamma \to 1$), energy in the summed feature is substantially attenuated; when directions are phase-aligned ($\gamma \to 0$), the original energy is largely preserved. In the final model, λ is fixed at its empirically determined optimal value of 0.2.

3 Experiments

3.1 Experimental Setup

DEM-Mamba is evaluated on four diverse datasets. BraTS2023 [29] (1251 MRIs) and BraTS2024 [30] (2200 MRIs) target composite tumor regions (WT, TC, ET) defined per official guidelines, plus resection-cavities (RC) for 2024. AIIB2023 [31] contains 120 HRCTs with complex airways, while the Cardiac Calcified Plaque Dataset, hosted by the Second Affiliated Hospital of Chongqing Medical University, includes 158 multi-parametric CTs for segmenting three anatomical regions:

Table 3: Comparison of Different Methods on Cardiac Calcified Plaque Datasets.

Method	Dice(%) ↑			HD95(mm) ↓		
	CB	ACP	CACP	CB	ACP	CACP
3D U-Net[24]	50.12	38.32	36.32	30.13	28.99	23.46
Swin UNETR[14]	52.82	39.33	35.62	24.36	21.56	21.45
CKD-TransBTS[25]	55.63	41.11	40.92	21.59	19.78	19.57
DAU-Net[26]	57.22	42.23	40.12	18.34	20.82	20.23
TransSea[27]	62.71	46.02	45.62	10.56	9.66	9.99
MAT[28]	60.62	44.42	43.92	12.45	10.56	10.50
VSMU-Net[18]	66.92	49.92	50.01	10.79	8.67	8.01
Proposed	**67.25**	**50.17**	**50.26**	**10.68**	**8.58**	**7.93**

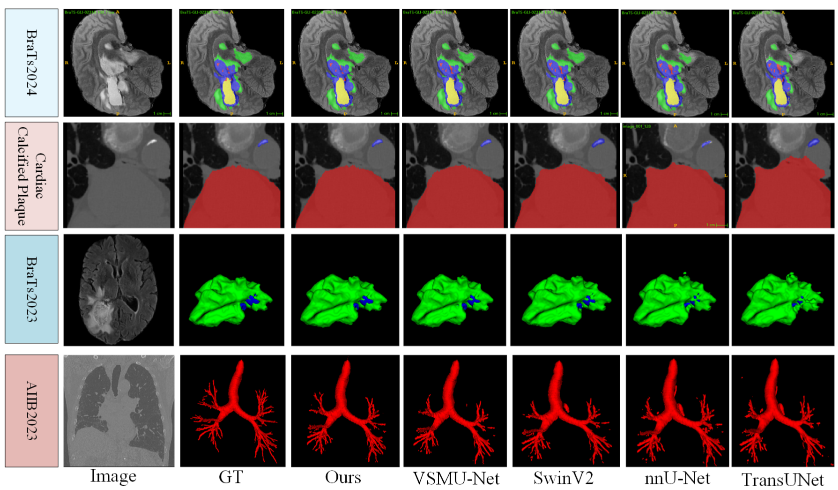

Fig. 3: Visualization results of different methods on the AIIB2023, BraTS2023, BraTS2024, and Cardiac Calcified Plaque Datasets.

cardiac background (CB), aortic plaque (ACP), and coronary artery plaque (CACP). All 128^3 cropped volumes undergo standard spatial/intensity augmentations with a 7:1:2 data split. Models are trained for 300 epochs on a single RTX 4090 using SGD (lr=1e-2) and a dynamic CE-Dice loss. We baseline against general 3D networks, including domain-specific SOTAs where applicable.

3.2 Comparison with State-of-the-arts

As shown in Tables 1–3, DEM-Mamba achieves the highest average Dice score of 91.43% for the key sub-regions (ET/TC/WT) on BraTS2023 and superior Dice scores on key sub-regions (WT/ET/RC) of BraTS2024, while also obtaining the best airway segmentation metrics on AIIB2023 and the highest Dice scores cou-

Table 4: The ablation experiments on the effect of different components were conducted on the BraTS2023 dataset.

Method	M1	M2	M3	Dice(%) ↑	HD95(mm) ↓
Baseline	×	×	×	90.23	3.62
Baseline + M1	✓	×	×	90.82	3.43
Baseline + M1+M2	✓	✓	×	91.32	3.35
Baseline + M1+M2+M3	✓	✓	✓	**91.43**	**3.23**

Table 5: Ablation studies on the BraTS2023 dataset.

(a) Order and Top-k of OAM.

Order	Top-k	DSC (% ↑)
2	1	90.01
2	2	**91.43**
2	3	91.16
1	2	90.07
3	2	90.47

(b) τ and λ.

Setting	λ	τ	DSC (% ↑)
Fixed best	0.2	0.1	91.38
Fixed λ, learnable τ	0.2	0.1	**91.43**
Fixed τ, learnable λ	0.2	0.1	91.00
w/o correction	-	-	91.32

pled with the lowest HD95 values for all sub-regions on the Cardiac Calcified Plaque dataset. Overall, these results demonstrate that DEM-Mamba consistently delivers state-of-the-art performance and strong generalization across diverse 3D medical image segmentation tasks (see Fig. 3 for qualitative examples).

3.3 Ablation Studies

(a) Module effectiveness analysis. As shown in Table 4, the baseline employs UNet with a unidirectional Mamba encoder. M1 incorporates an OAM module to weight and fuse controllable high-frequency directional components. M2 further introduces BBM to enhance cross-directional sequence dependency modeling. Finally, the OCF module (M3) replaces the original fusion strategy, yielding optimal results (average Dice across ET/TC/WT: 91.43%, mean HD95: 3.23 mm).

(b) Parameter Ablation Study. As shown in Table 5 (a) and (b), in ablation experiments, when Order=2, Top-K=2, and τ is set as a learnable parameter (initial value 0.1) while fixing $\lambda = 0.2$, the model achieves the highest average DSC value of 91.43%. This result outperformed other Order and Top-K configurations, parameter settings with fixed τ and λ, as well as DEM-Mamba without the correction module(OCF).

4 Conclusion

This paper proposes DEM-Mamba, a direction-aware balanced Mamba network for 3D medical image segmentation. By decoupling structural orientations via learnable Riesz steerable wavelets and adaptively fusing complementary bidirectional scans, DEM-Mamba improves anisotropic perception and boundary accuracy. Across four 3D datasets, DEM-Mamba outperforms state-of-the-art methods by reducing scan bias and boundary blur. Future work will improve generalization and further integrate state-space with frequency-domain directional modeling.

Acknowledgments. This work was supported by the National Natural Science Foundation of China (62576062, 62576132, U23A20294); in part by the Science and Technology Research Program of Chongqing Municipal Education Commission under Grant KJZD-M202500604; in part by the New Chongqing Youth Innovation Talent Program under Grant CSTB2024NSCQ-QCXMX0067; in part by the Central Government Program for Guiding Local Regional Innovation System Development Project under Grant 202502ZYDF029; in part by the Science and Technology Innovation Key R&D Program of Chongqing under Grant CSTB2024TIAD-STX0023; and in part by the Chongqing Municipal Special Program for Technological Innovation and Application Development under Grant CSTB2024TIAD-GPX0015.

Disclosure of Interests. The authors have no competing interests to declare that are relevant to the content of this article.

References

1. Zou, K., Lin, T., Yuan, X., et al.: Reliable multimodality eye disease screening via mixture of student's t distributions. In: Medical Image Computing and Computer Assisted Intervention – MICCAI 2023. vol. 14226, pp. 596–606 (2023)
2. Zhou, N., Zou, K., Ren, K., et al.: MedSAM-U: Uncertainty-guided auto multi-prompt adaptation for reliable MedSAM. IEEE Transactions on Circuits and Systems for Video Technology **36**(3), 3768–3781 (2026)
3. Zou, K., Lin, T., Han, Z., et al.: Confidence-aware multi-modality learning for eye disease screening. Medical Image Analysis **96**, 103214 (2024)
4. Ma, Y., Liu, Y., Cheng, J., et al.: CIHM: Context-insight hybrid Mamba for efficient medical image segmentation. Visual Intelligence **4**(1), 12 (2026)
5. Zou, K., Bai, Y., Chen, Z., et al.: Uncertainty-aware medical diagnostic phrase identification and grounding. IEEE Transactions on Pattern Analysis and Machine Intelligence **47**(12), 11315–11329 (2025)
6. Sun, J., Chen, K., Wu, X., et al.: MSM-UNet: A medical image segmentation method based on wavelet transform and multi-scale Mamba-UNet. Expert Systems with Applications **288**, 128241 (2025)
7. Zou, K., Chen, Y., Huang, L., et al.: Toward reliable medical image segmentation by modeling evidential calibrated uncertainty. IEEE Transactions on Cybernetics **55**(12), 5975–5988 (2025)

8. Chenouard, N., Unser, M.: 3d steerable wavelets in practice. IEEE Transactions on Image Processing **21**(11), 4522–4533 (2012)
9. Wang, Q., Wu, B., Zhu, P., et al.: ECA-Net: Efficient channel attention for deep convolutional neural networks. In: Proceedings of the IEEE/CVF Conference on Computer Vision and Pattern Recognition. pp. 11531–11539 (2020)
10. Andreescu, T., Feng, Z.: Inclusion-exclusion principle. In: A Path to Combinatorics for Undergraduates: Counting Strategies, pp. 117–141 (2004)
11. Isensee, F., Jaeger, P.F., Kohl, S.A., et al.: nnU-Net: A self-configuring method for deep learning-based biomedical image segmentation. Nature Methods **18**(2), 203–211 (2021)
12. Chen, J., Mei, J., Li, X., et al.: TransUNet: Rethinking the U-Net architecture design for medical image segmentation through the lens of transformers. Medical Image Analysis **97**, 103280 (2024)
13. Hatamizadeh, A., Tang, Y., Nath, V., et al.: UNETR: Transformers for 3d medical image segmentation. In: Proceedings of the IEEE/CVF Winter Conference on Applications of Computer Vision. pp. 1748–1758 (2022)
14. Hatamizadeh, A., Nath, V., Tang, Y., et al.: Swin UNETR: Swin transformers for semantic segmentation of brain tumors in MRI images. arXiv preprint arXiv:2201.01266 (2022)
15. Roy, S., Koehler, G., Ulrich, C., et al.: MedNeXt: Transformer-driven scaling of ConvNets for medical image segmentation. In: Medical Image Computing and Computer Assisted Intervention – MICCAI 2023. vol. 14223, pp. 405–415 (2023)
16. He, Y., Nath, V., Yang, D., et al.: SwinUNETR-V2: Stronger Swin transformers with stagewise convolutions for 3d medical image segmentation. In: Medical Image Computing and Computer Assisted Intervention – MICCAI 2023. vol. 14223, pp. 416–426 (2023)
17. Wu, R., Liu, Y., Ning, G., et al.: UltraLight VM-UNet: Parallel vision Mamba significantly reduces parameters for skin lesion segmentation. Patterns **6**(11), 101298 (2025)
18. Zhu, Z., Wang, Z., Qi, G., et al.: Visually stabilized Mamba U-Shaped network with strong inductive bias for 3-d brain tumor segmentation. IEEE Transactions on Instrumentation and Measurement **74**, 1–11 (2025)
19. Liu, Z., Lin, Y., Cao, Y., et al.: Swin transformer: Hierarchical vision transformer using shifted windows. In: Proceedings of the IEEE/CVF International Conference on Computer Vision. pp. 9992–10002 (2021)
20. Wang, W., Chen, C., Ding, M., et al.: TransBTS: Multimodal brain tumor segmentation using transformer. In: Medical Image Computing and Computer Assisted Intervention – MICCAI 2021. vol. 12901, pp. 109–119 (2021)
21. Xing, Z., Yu, L., Wan, L., et al.: NestedFormer: Nested modality-aware transformer for brain tumor segmentation. In: Medical Image Computing and Computer Assisted Intervention – MICCAI 2022. vol. 13435, pp. 140–150 (2022)
22. Zhou, H.Y., Guo, J., Zhang, Y., et al.: nnFormer: Volumetric medical image segmentation via a 3d transformer. IEEE Transactions on Image Processing **32**, 4036–4045 (2023)
23. Zheng, S., Ye, X., Yang, C., et al.: Asymmetric adaptive heterogeneous network for multi-modality medical image segmentation. IEEE Transactions on Medical Imaging **44**(4), 1836–1852 (2025)
24. Çiçek, Ö., Abdulkadir, A., Lienkamp, S.S., et al.: 3D U-Net: Learning dense volumetric segmentation from sparse annotation. In: International Conference on Medical Image Computing and Computer-Assisted Intervention. pp. 424–432 (2016)

25. Lin, J., Lin, J., Lu, C., et al.: CKD-TransBTS: Clinical knowledge-driven hybrid transformer with modality-correlated cross-attention for brain tumor segmentation. IEEE Transactions on Medical Imaging **42**(8), 2451–2461 (2023)
26. Hsieh, Y.A., Tsai, Y.C.J.: DAU-Net: Dense attention U-Net for pavement crack segmentation. In: 2021 IEEE International Intelligent Transportation Systems Conference (ITSC). pp. 2251–2256 (2021)
27. Liu, Y., Ma, Y., Zhu, Z., et al.: TransSea: Hybrid CNN-transformer with semantic awareness for 3-d brain tumor segmentation. IEEE Transactions on Instrumentation and Measurement **73**, 16–31 (2024)
28. Baid, U., Ghodasara, S., Mohan, S., et al.: The RSNA-ASNR-MICCAI BraTS 2021 benchmark on brain tumor segmentation and radiogenomic classification. arXiv preprint arXiv:2107.02314 (2021)
29. Bakas, S., Akbari, H., Sotiras, A., et al.: Advancing the cancer genome atlas glioma MRI collections with expert segmentation labels and radiomic features. Scientific Data **4**(1), 1–13 (2017)
30. de Verdier, M.C., Saluja, R., et al.: The 2024 brain tumor segmentation (BraTS) challenge: Glioma segmentation on post-treatment MRI. arXiv preprint arXiv:2405.18368 (2024)
31. Nan, Y., Xing, X., Wang, S., et al.: Hunting imaging biomarkers in pulmonary fibrosis: Benchmarks of the AIIB23 challenge. Medical Image Analysis **97**, 103253 (2024)